
Article:
Bruckbauer, J., Trager-Cowan, C., Hourahine, B. et al. (2020) Luminescence behavior of semipolar (101¯1) InGaN/GaN “bow-tie” structures on patterned Si substrates. Journal of Applied Physics, 127 (3). ISSN: 0021-8979

https://doi.org/10.1063/1.5129049

Journal of Applied Physics

Luminescence behavior of semipolar (10 $\bar{1}$ 1) InGaN/GaN "bow-tie" structures on patterned Si substrates

Cite as: J. Appl. Phys. **127**, 035705 (2020); https://doi.org/10.1063/1.5129049
Submitted: 24 September 2019 . Accepted: 14 December 2019 . Published Online: 17 January 2020

Jochen Bruckbauer, Carol Trager-Cowan, Ben Hourahine, Aimo Winkelmann, Philippe Vennéguès, Anja Ipsen, Xiang Yu, Xunming Zhao, Michael J. Wallace, Paul R. Edwards, G. Naresh-Kumar, Matthias Hocker, Sebastian Bauer, Raphael Müller, Jie Bai, Klaus Thonke, Tao Wang, and Robert W. Martin

COLLECTIONS

Paper published as part of the special topic on Defects in Semiconductors 2020
Note: This paper is part of the Special Topic on Defects in Semiconductors 2020.

This paper was selected as Featured

Journal of Applied Physics ARTICLE scitation.org/journal/jap

Luminescence behavior of semipolar $(10\bar{1}1)$ InGaN/GaN "bow-tie" structures on patterned Si substrates

Cite as: J. Appl. Phys. **127**, 035705 (2020); doi: 10.1063/1.5129049
Submitted: 24 September 2019 · Accepted: 14 December 2019 ·
Published Online: 17 January 2020

View Online Export Citation CrossMark

Jochen Bruckbauer,[1,a)] Carol Trager-Cowan,[1] Ben Hourahine,[1] Aimo Winkelmann,[1,2] Philippe Vennéguès,[3] Anja Ipsen,[4] Xiang Yu,[5] Xunming Zhao,[5] Michael J. Wallace,[1] Paul R. Edwards,[1] G. Naresh-Kumar,[1] Matthias Hocker,[4] Sebastian Bauer,[4] Raphael Müller,[4] Jie Bai,[5] Klaus Thonke,[4] Tao Wang,[5] and Robert W. Martin[1]

AFFILIATIONS

[1]Department of Physics, SUPA, University of Strathclyde, Glasgow G4 0NG, United Kingdom
[2]Laser Zentrum Hannover e.V., D-30419 Hannover, Germany
[3]CNRS-CRHEA, Université Côte d'Azur, 06560 Valbonne, France
[4]Institute of Quantum Matter, Ulm University, D-89081 Ulm, Germany
[5]Department of Electronic and Electrical Engineering, University of Sheffield, Sheffield S1 3JD, United Kingdom

Note: This paper is part of the Special Topic on Defects in Semiconductors 2020.
[a)]**Electronic mail:** jochen.bruckbauer@strath.ac.uk

ABSTRACT

In this work, we report on the innovative growth of semipolar "bow-tie"-shaped GaN structures containing InGaN/GaN multiple quantum wells (MQWs) and their structural and luminescence characterization. We investigate the impact of growth on patterned (113) Si substrates, which results in the bow-tie cross section with upper surfaces having the $(10\bar{1}1)$ orientation. Room temperature cathodoluminescence (CL) hyperspectral imaging reveals two types of extended defects: black spots appearing in intensity images of the GaN near band edge emission and dark lines running parallel in the direction of the Si stripes in MQW intensity images. Electron channeling contrast imaging (ECCI) identifies the black spots as threading dislocations propagating to the inclined $(10\bar{1}1)$ surfaces. Line defects in ECCI, propagating in the $[1\bar{2}10]$ direction parallel to the Si stripes, are attributed to misfit dislocations (MDs) introduced by glide in the basal (0001) planes at the interfaces of the MQW structure. Identification of these line defects as MDs within the MQWs is only possible because they are revealed as dark lines in the MQW CL intensity images, but not in the GaN intensity images. Low temperature CL spectra exhibit additional emission lines at energies below the GaN bound exciton emission line. These emission lines only appear at the edge or the center of the structures where two (0001) growth fronts meet and coalesce (join of the bow-tie). They are most likely related to basal-plane or prismatic stacking faults or partial dislocations at the GaN/Si interface and the coalescence region.

I. INTRODUCTION

Over half a century ago, silicon revolutionized the semiconductor industry through its use in transistors and integrated circuits.[1,2] Decades later, it may be said that another revolution occurred, but this time in the field of solid-state lighting, through the advances of III-nitride semiconductors and their applications in light-emitting diodes (LEDs) and high power transistors.[3] Commercial nitride optoelectronic devices are commonly grown on sapphire substrates along the polar *c*-direction. Although the success of these substrates is undeniable in the blue spectral range, using Si as a substrate might offer several advantages. Growing nitride-based LEDs on Si makes it possible to combine them with existing, mature, and well-developed Si technologies such as CMOS (complementary metal–oxide–semiconductor) drivers and

integrated circuits as control electronics for the LEDs. Apart from Si being a cost-effective substrate for the growth, the exploitation of existing Si-based processing facilities and wafer scalability makes this an inexpensive alternative to sapphire.

It is also well known that the internal electric fields, which are strongest in the polar *c*-/[0001]-direction, are a contributing factor for reduced device efficiencies and become stronger for longer emission wavelengths.[4,5] Nonpolar and semipolar orientations are one possibility for either eliminating or reducing the influence of the quantum-confined Stark effect (QCSE) caused by these built-in electric fields.[6,7] Furthermore, using Si as a substrate makes it fairly easy to explore different crystal orientations for the growth of GaN.[8] The best crystallographic alignment, with a lattice mismatch of about 17%, is for the growth of (0001) GaN on (111) Si.[8] In order to access semipolar orientations, the angles between the (0001) GaN plane and the different {111} Si facets are important. For the growth of GaN on (113) Si substrates, the $(11\bar{2}2)$ GaN orientation can be accessed through growth on the $(\bar{1}11)$ or $(1\bar{1}1)$ Si facets and the $(20\bar{2}1)$ GaN orientation through growth on the $(\bar{1}\bar{1}1)$ Si facet, although the latter will have a slight offset angle of 4.89° from the true surface normal (see Fig. 1).[9]

The growth of GaN on Si raises several problems, which need to be overcome. The Si surface is susceptible to oxidation, which means that before growth commences, the oxidized layer needs to be removed.[10] At the usual GaN growth temperatures, Ga also strongly reacts with Si forming a eutectic alloy.[11] This causes strong etching of the material, referred to as "melt-back etching."[12] In addition to the lattice mismatch, another major issue is the mismatch in thermal expansion coefficients (≈46%) between GaN and Si. They both produce tensile strain, leading to wafer cracking and bowing, which is more pronounced compared with sapphire substrates.[13] The large lattice mismatch is also responsible for a high density of threading dislocations (TDs), which in turn lowers the internal quantum efficiency.[14]

In this paper, we describe the investigation of extended defects in semipolar III-nitride materials produced by growth on patterned (113) Si substrates. We investigate the optical and structural properties of semipolar InGaN/GaN multiple quantum wells (MQWs) grown on GaN "bow-tie" structures with $\{10\bar{1}1\}$ top surfaces. The cross-sectional bow-tie shape, as seen in Fig. 1, is due to the patterning of the Si substrate and the subsequent growth of GaN on the {111} family of planes of Si. Cathodoluminescence (CL) hyperspectral imaging shows areas of nonradiative recombination associated with extended defects at room temperature and emission lines related to stacking faults at low temperature. These defects, giving rise to nonradiative recombination at room temperature, were identified as threading dislocations (TDs) and misfit dislocations (MDs) using electron channeling contrast imaging (ECCI).

II. EXPERIMENTAL SECTION

The fabrication of the structures is a two-step process. The first step is a patterning of the Si substrate, which is followed by the growth of GaN using metal-organic chemical vapor deposition (MOCVD).

The (113) Si substrate is patterned into 5.5 μm wide and 4.5 μm deep stripes along the $[1\bar{1}0]$ direction. Initially, a 120 nm thick SiO_2 layer is deposited on the substrate using plasma-enhanced chemical vapor deposition. Afterward, a standard photolithography process is applied to create stripes of photoresist followed by the deposition of Ni using a thermal evaporator. After a lift-off process, the Ni stripes are used as a secondary mask to etch the Si substrate using reactive ion etching and inductively-coupled plasma etching techniques. Subsequently, the Ni mask is removed. In order to achieve {111} Si facets, the patterned Si is anisotropically etched in a KOH solution (25 wt. %) at a temperature of 30 °C.

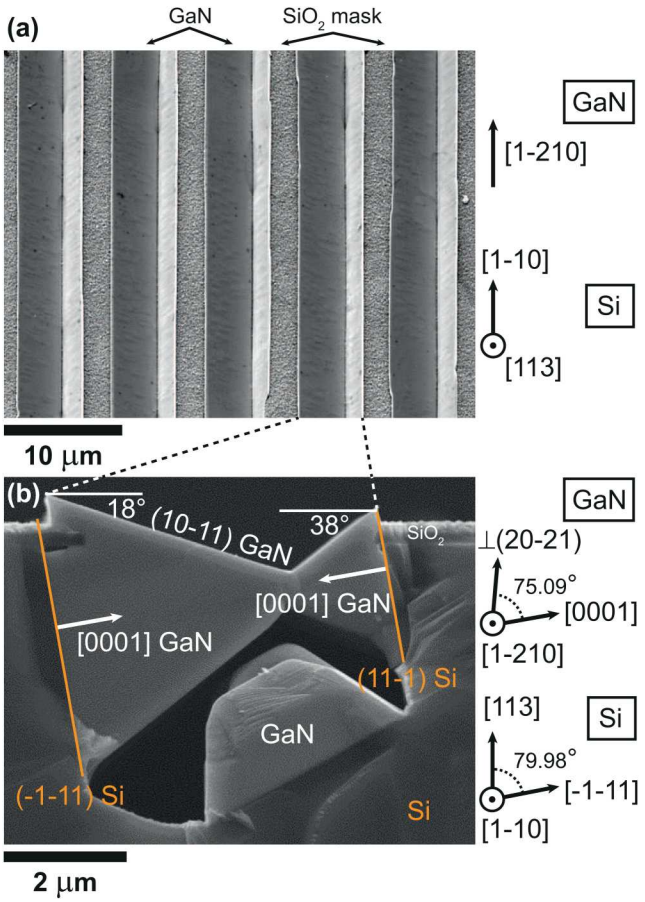

FIG. 1. (a) Top-view and (b) cross-sectional SE images of the GaN "bow-tie" structure on the Si structure. The near vertical orientation of the GaN is $(20\bar{2}1)$, which is tilted away by 4.89° from the (113) Si substrate plane.

The MOCVD growth of the structure starts with the deposition of a 100 nm thick, high temperature AlN buffer layer. This prevents the melt-back issue of GaN on Si. Next, the growth of (0001) GaN on the facets is initiated until the growth fronts from the $(\bar{1}\bar{1}1)$ and $(11\bar{1})$ facets meet and coalesce. A 5-period InGaN/GaN MQW structure is then grown on top of the GaN. The nominal thicknesses of the InGaN quantum wells and GaN barriers are 2 nm and 12 nm, respectively. The final layer is a GaN barrier. Figure 1(a) shows a top-view secondary electron (SE) image of the resulting structure.

The crystallographic orientations of the structure were determined by high resolution X-ray diffraction (HRXRD). As seen in the SE image in Fig. 1(b), the cross section of the structure is similar to the shape of a bow-tie with the MQWs located at the two inclined top surfaces. GaN grows with a triangular cross section along the [0001] direction on both the equivalent $(\bar{1}\bar{1}1)$ and $(11\bar{1})$ Si facets, resulting in two (0001) GaN growth fronts approaching each other until they meet and coalesce at the "join" of the bow-tie. The (0001) orientation of the two opposing GaN segments was confirmed by electron backscatter diffraction (shown in Sec. S1 of the supplementary material). This confirms that both growth fronts are of Ga-/(0001) polarity. However, since the two growth segments grow toward one another, they have opposite polarity with respect to each other. When the two (0001) growth fronts meet, they coalesce and form an antiphase domain boundary at the join of the bow-tie. The angles between the horizontal plane and the two inclined MQW/GaN surfaces are approximately 18° and 38° as seen in Fig. 1(b). A χ-dependent HRXRD measurement (tilted away from the surface plane) of the asymmetric $\{10\bar{1}1\}$ GaN planes confirms these angles and that the orientation of these planes is $\{10\bar{1}1\}$. The $(10\bar{1}1)$ orientation is the most stable one during MOCVD growth due to its lower growth rate, which potentially benefits crystal quality and surface morphology.[15] A more detailed analysis on the HRXRD results can be found in Sec. S2 of the supplementary material.

Room temperature CL measurements were carried out in a variable pressure field emission gun scanning electron microscope (SEM, FEI Quanta 250). The light emitted from the sample, which is tilted by 45°, is collected by a Schwarzschild reflecting objective with its optical axis perpendicular to the direction of the electron beam, then dispersed with a 1/8 m focal length spectrometer (Oriel MS125), and collected using a 1600-channel electron multiplying charge-coupled device (CCD, Andor Newton).[16,17] Low temperature CL was performed in a field emission gun SEM (Zeiss LEO DSM 982) equipped with custom-built liquid helium flow cryostage (CryoVac). The light was collected using a UV-enhanced glass fiber placed in close contact with the sample, dispersed with a 90 cm focal length monochromator (SPEX 1702), and detected using a liquid nitrogen-cooled, UV-optimized CCD.[18] In both microscopes, the CL was collected in hyperspectral imaging mode, where a spectrally-resolved luminescence spectrum is collected for every pixel in the image. The room temperature and low temperature (≈12 K)

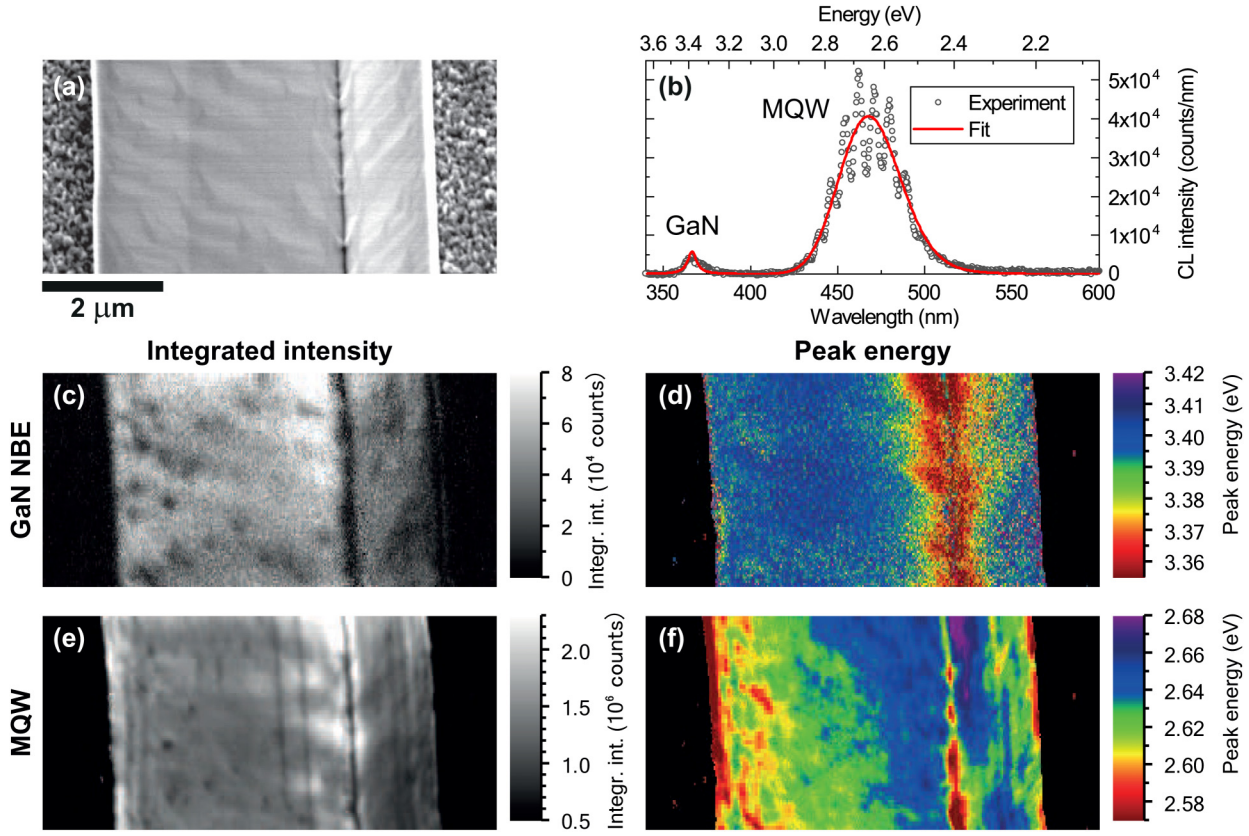

FIG. 2. Plan-view CL imaging of the tilted $(10\bar{1}1)$ top surfaces: (a) SE image and (b) example spectrum with numerical fit. The CL images were generated through peak fitting: (c) integrated intensity and (d) peak energy of the GaN NBE emission and (e) integrated intensity and (f) peak energy of the MQW emission. The scale bar in (a) applies to all CL images.

measurements were acquired with a beam voltage of 5 kV. The images presented here are generated from the hyperspectral dataset by either least-squares peak fitting (using Gaussian and Voigt functions) or plotting intensity images of selected wavelength ranges.

ECCI is a nondestructive diffraction technique performed in the SEM to identify extended defects.[19,20] ECCI micrographs are generally constructed by measuring the intensity of the backscattered electrons as the electron beam scans across the surface of a suitably-orientated sample. The sample is positioned so that a plane or planes in the sample are at, or close to, their Bragg angle, which allows electrons entering the sample to be diffracted providing the dominant structural contrast in the image. Any changes in crystallographic orientation and local strain can be monitored by the variation in the intensity of the backscattered electrons causing a change in contrast in an ECCI micrograph. This allows the imaging of low-angle tilt and rotation boundaries, atomic steps, and extended defects (e.g., TDs or stacking faults).[20,21] ECCI was carried out in a forward scattering geometry in a field emission SEM (FEI Sirion 200), equipped with an electron-sensitive diode and a custom-built signal amplifier. All the ECCI micrographs were acquired with an electron beam energy of 30 keV and a sample tilt of around 50° relative to the incident beam normal.

III. RESULTS AND DISCUSSION

CL imaging at room temperature was carried out in two different geometries (top view and cross-section) due to the three-dimensional structure of the sample. The results are presented in Figs. 2 and S4 (Sec. S3 in the supplementary material).

In order to investigate the emission properties of the inclined $(10\bar{1}1)$ surfaces, which are tilted by about 18° and 38° from the surface of the substrate as seen in Fig. 1(b), a measurement of the sample top surface was performed. The SE micrograph in Fig. 2(a) shows the area that was imaged by CL, which is a smaller area of the top surface of the sample as seen in Fig. 1(a). The rough areas on the left-hand side and right-hand side in the SE image are regions where the SiO_2 mask, used for etching the stripes into the Si substrate, is still exposed. The single vertical black line is the join of the bow-tie where the two opposing (0001) GaN growth fronts meet and coalesce. Figure 2(b) shows an example CL spectrum, which consists of two emission peaks. One is associated with the near band edge (NBE) emission from the underlying GaN and the other arises from the 5-period MQW structure grown on the $(10\bar{1}1)$ surfaces. To generate two-dimensional CL images, each spectrum in the CL dataset was fitted with a Voigt and Gaussian function for the GaN NBE and MQW peaks, respectively. The integrated intensity and peak energy for the GaN NBE and MQW peaks are displayed in Figs. 2(c) and 2(d) and Figs. 2(e) and 2(f), respectively.

The intensity distribution of the GaN NBE peak is fairly uniform except for the appearance of black spots and a dark line as seen in the GaN intensity image in Fig. 2(c). This single vertical dark line corresponds to the region where the two opposing (0001) growth fronts with Ga-polarity meet. Since two Ga-polar growth fronts approach each other from opposite directions, i.e., the two growth fronts have different polarities with respect to each other, this region also forms an antiphase domain boundary. Nonradiative recombination at this antiphase domain boundary leads to its dark appearance in the CL intensity images at the join of the bow-tie.[22] Similarly, the GaN peak energy image [Fig. 2(d)] shows a fairly uniform distribution on the $(10\bar{1}1)$ surface, except near the join region where the peak is redshifted. This shift is indicative of a change in strain in the join region, where the GaN is either less compressively or more tensilely strained. The black spots are a common phenomenon and are associated with nonradiative recombination at TDs,[23] as further discussed for the ECCI results shown in Fig. 5.

The CL images generated from the MQW peak are slightly more complex. Although the MQW intensity is mostly uniform [Fig. 2(e)], there are faint dark lines parallel to the stripes of the mask and dark spots present. Most of the dark spots correlate to the dark spots already observed in the GaN intensity image in Fig. 2(c) associated with threading dislocations. Similarly, the join appears as a dark line in the MQW intensity image. The length of these faint dark lines varies and is estimated to be $3-4\,\mu$m, based on several CL images. They are likely to be misfit dislocations, which appear as dark lines in pan- and monochromatic CL images in semipolar and nonpolar III-nitride structures[24–26] and will be discussed further with the ECCI results. Similar $(1\bar{1}01)$ InGaN/GaN MQW structures were investigated in Ref. 27. They attributed the dark lines in panchromatic CL images to stacking faults and misfit dislocations

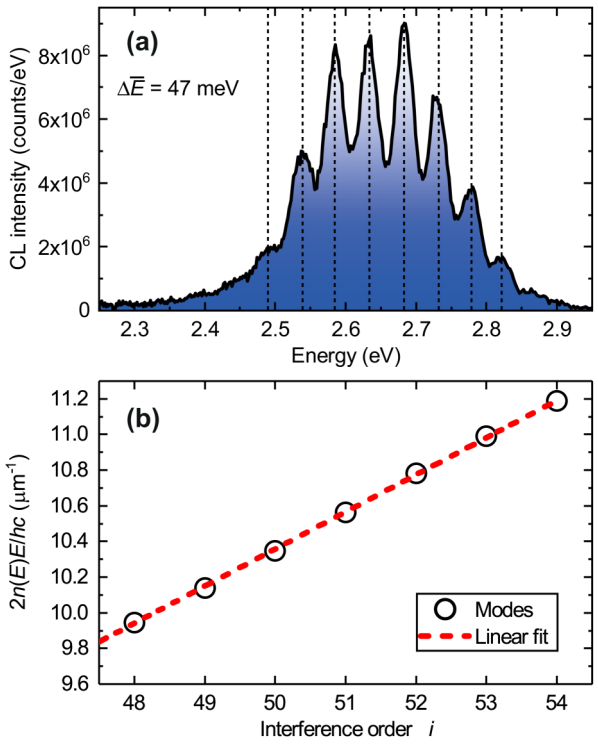

FIG. 3. (a) Example CL spectrum with Fabry–Pérot interference fringes superimposed on the MQW emission peak. The spectrum is the same as shown in Fig. 2(b), but it is only showing the region of the MQW emission on an energy scale. (b) Graphical representation of Eq. (1) using the peak position of the modes shown in Fig. 3(a).

generated due to strain relaxation. The density of the dark lines also increased with the InN content of the InGaN/GaN MQWs meaning that the larger strain in the higher InN containing samples was released by the generation of more of these defects.

CL on the cross-section (shown in Sec. S3 of the supplementary material) confirmed that the MQW structure is located only at the top $(10\bar{1}1)$ surface planes. Only the GaN NBE emission is observed below the top surface. The CL image of the MQW peak energy, displayed in Fig. 2(f), shows lateral shifts in energy in the order of 100 meV. These energy shifts are more dominant closer to the dark lines (misfit dislocations) and hence may be strain related as discussed previously.

Closer examination of the individual CL spectra from the hyperspectral dataset revealed sharp peaks superimposed on the MQW emission, as seen in Fig. 3(a). The peak separation is approximately constant with a mean energy separation $\Delta\bar{E}$ of 47 meV. An optical path length L of about 5.3 μm can be calculated using the simple equation $L = \frac{hc}{2n\Delta E}$ using a refractive index of $n = 2.45$ for GaN, taken as a constant over this spectral range. This matches well with the stripe width of 5.5 μm in the patterned Si substrate, as also seen in the SE image in Fig. 1(b). The change in the refractive index between the GaN and the {111} Si sidewalls causes the width of the groove to act as an optical cavity giving rise to these Fabry–Pérot interference fringes. Alternatively, the cavity size can be calculated more accurately from the slope of the curve in Fig. 3(b) following Ref. 28, which is a graphical representation of the following equation and also takes the energy-dependent refractive index into account:

$$i\frac{1}{d} = \frac{2n(E)E}{hc}, \tag{1}$$

where i is the interference order, E the energy position of the modes, and $n(E)$ the energy-dependent refractive index. The room temperature refractive index $n(E)$ as a function of emission energy was calculated using a Sellmeier function from Ref. 29. A linear fit of the data in Fig. 3(b) yields a cavity size of $d = 4.8\,\mu$m. The real interference order i was calculated using the above equation once the cavity size d was determined. Ideally, this should provide a more accurate value for the cavity width since the energy dependence of the refractive index was taken into account. The cavity size is about 12% smaller than the actual Si stripe width, which could be due to several reasons. The actual width of the cavity could be smaller than the width of the patterned Si substrate due to slight differences in the patterning. Also, the light has to pass through the entire structure to reach either interface, which means that it has to pass through the center of the bow-tie. This is where the two c-plane growth fronts meet and coalesce, leading to an antiphase domain boundary as seen as a dark line in the top-view CL intensity images in Figs. 2(c) and 2(e), where the join appears as a black line of reduced intensity. The generation of the modes is, therefore, most likely more complicated than the assumed internal reflection on the GaN/Si interface and the light propagation.

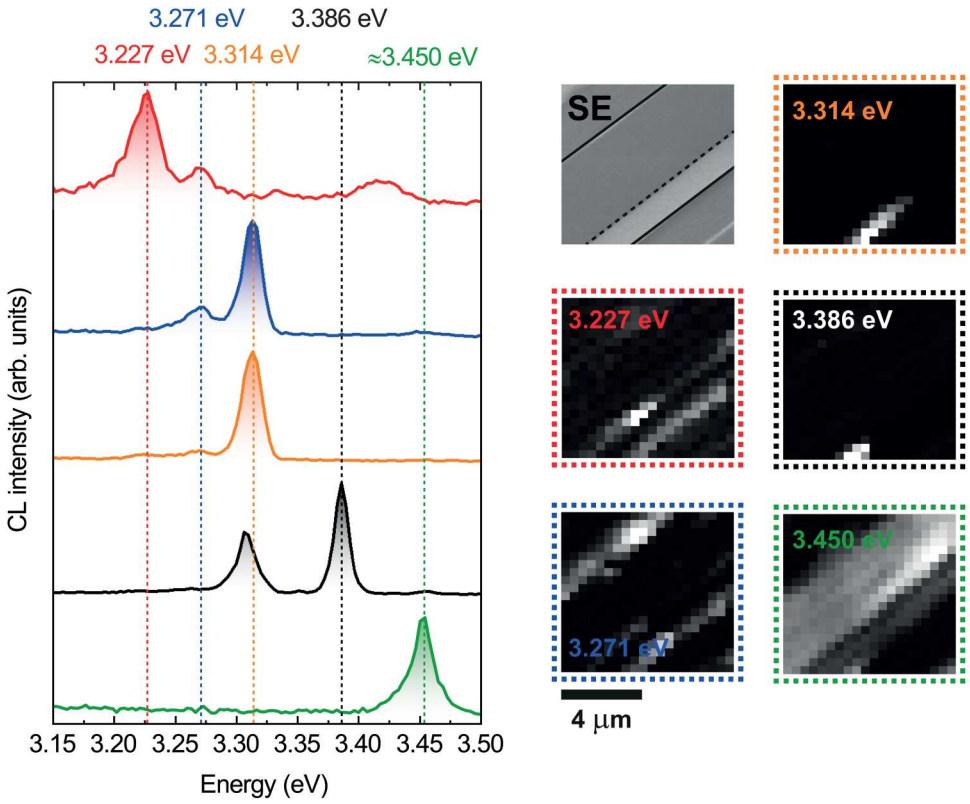

FIG. 4. Low temperature (≈12 K) CL spectra showing emission peaks around 3.227 eV, 3.271 eV, 3.314 eV, and 3.386 eV in addition to the emission peak of the GaN bound exciton (3.450 eV). The insets on the right show the corresponding integrated CL intensity images of these emission peaks with the SE image of the same area at the top. The edges (solid line) and the join (dashed) in the bow-tie structure are marked by lines in the SE image.

Figure 4 displays example CL spectra extracted from the hyperspectral dataset recorded at low temperature (≈12 K). The insets show the corresponding integrated CL intensity images of the selected emission peaks, i.e., 3.227 eV, 3.271 eV, 3.314 eV, 3.386 eV, and 3.450 eV (bound exciton) and the SE image of the measured area. For semi- and nonpolar GaN, low temperature emission peaks below the bound exciton peaks in the region of 3.25−3.40 eV are often observed and associated with different extended defects, such as basal-plane stacking faults (BSFs), prismatic stacking faults (PSFs), and partial dislocations (PDs).[30–36] The four emission peaks, as shown in the corresponding CL intensity images in the insets of Fig. 4, appear either on the edge or the join of the bow-tie structure. The join is the region where the two $+c$/(0001)-growth fronts meet and coalesce, leading to a defected

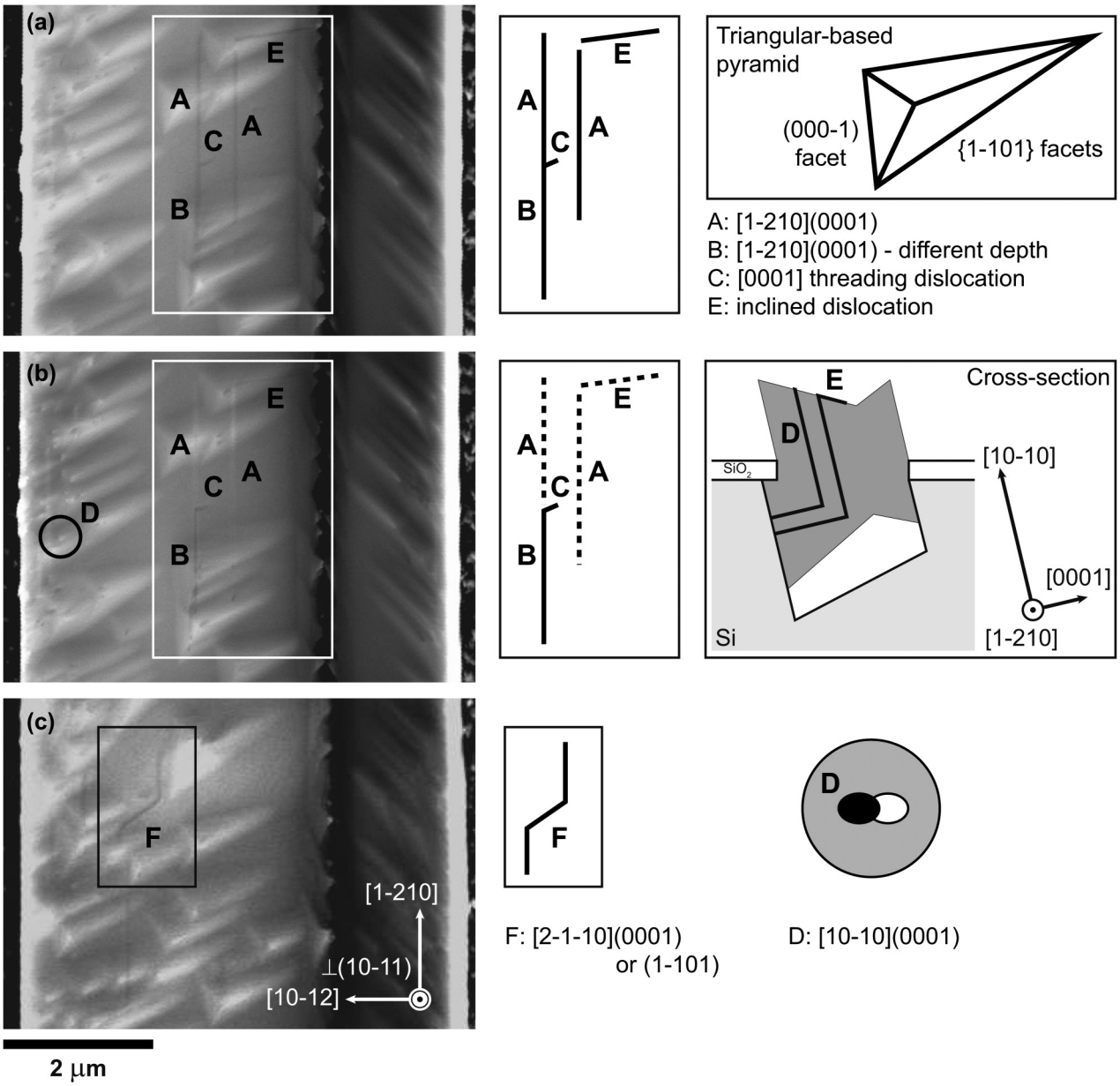

FIG. 5. (a) and (b) ECCI micrographs from the same area acquired at two different diffraction conditions by slightly rotating the sample. The different defects are marked by letters "A," "B," "C," "D," and "E" and are schematically shown on the right of the figure. (c) ECCI micrograph from a different area illustrating defect "F." The scale bar and directions in (c) apply to all ECCI micrographs.

region (antiphase domain boundary), which appears as a black line in the room temperature CL images in Figs. 2(c) and 2(e) due to nonradiative recombination at this temperature. The edges of the structure correspond to the region where the growth on the {111} Si facets is initiated, leading to defects at the GaN/Si interface due to the mismatch in lattice constants and thermal expansion coefficients. Transmission electron microscope (TEM) measurements (shown in Sec. S4 of the supplementary material) show that dislocations are predominantly observed at the GaN/Si interface. Continued growth leads to dislocation reduction due to defect interaction or dislocation bending, resulting in very few dislocations reaching the surface as shown by the small density of dark spots in the GaN intensity image in Fig. 2(c). The appearance of the additional emission peaks below the GaN bound exciton emission on the edge of the bow-tie structure, as seen in the low temperature CL intensity images in the insets of Fig. 4, also indicate that the TDs and possibly BSFs are confined to the region of the GaN/Si interface. At low temperature, stacking faults can act as quantum wells due to the insertion of a thin layer of zinc-blende material with a lower bandgap into the wurtzite lattice of larger bandgap. It is important to note that the emission peaks associated with BSF emission do not have a fixed energy, because these QW-like structures are also influenced by spontaneous/piezoelectric polarization fields, leading to shifts in their energy position.[30] This suggests that these four observed emission peaks are associated with different stacking faults, e.g., prismatic and basal-plane stacking faults.[30–36] Furthermore, comparison with the literature suggests different possible causes for the emission around 3.27 eV. It may be related to partial dislocations terminating BSFs[31,32] or a donor–acceptor-pair transition.[37] The stacking faults may also lead to slightly larger zinc-blende inclusions where the emission is not dominated by the QW-like behavior but rather by the excitonic emission from the zinc-blende material.[38]

In order to investigate these structural properties further, ECCI was performed on the inclined top surfaces. While ECCI is an excellent technique for quantification of extended defects that reach the surface, it is harder to detect and quantify dislocations below the surface due to the surface sensitivity of ECCI and the difficulty in determining the precise sampling depth of the technique. It is possible, however, to image dislocations that lie below, but *close* to the surface, as illustrated in Ref. 39 for misfit dislocations in GaP grown on Si located at up to around 100 nm from the surface.

Figure 5 shows three top-view ECCI micrographs acquired from the sample. Figures 5(a) and 5(b) were acquired from close to the same part of the sample, but at different diffraction conditions. It was not possible to determine the exact diffraction conditions for these ECCI micrographs; however, the diffraction condition can be changed by a small rotation of about 0.2° of the sample. Due to the tilt of the sample, strong topographic contrast is obtained in addition to diffraction contrast. The images reveal that the $(10\bar{1}1)$ surfaces are not smooth but are covered with triangular-based pyramids. Following the work reported in Ref. 40, we tentatively identify the facets of these features as $(000\bar{1})$ and $\{1\bar{1}01\}$ planes. Such hillock structures generally form as a result of spiral growth around dislocations with a screw component. When growth is on the $(10\bar{1}1)$ plane, they exhibit the observed triangular-based pyramid structure.[41]

The line features running parallel to the $[1\bar{2}10]$ direction (vertical in Fig. 5) are identified from the literature as most likely to be misfit dislocations introduced by glide in the basal (0001) planes at the interfaces of the MQW structure.[25,42,43] Note that the misfit dislocations labeled "A" change contrast from black to white on changing the diffraction condition, while the misfit dislocation labeled "B" does not. This indicates that the "A" dislocations have opposite Burgers vectors or lie at a different depth compared with the "B" dislocations. Identification of these line defects as misfit dislocations is only possible because they are revealed as dark lines in the CL intensity images of the MQW emission [Fig. 2(e)] but not in GaN intensity images [Fig. 2(c)]. Dislocation B propagates in the $[1\bar{2}10]$ direction and then changes direction (as shown as dislocation segment labeled "C"). In comparison with the $(000\bar{1})$ facets of the triangular-based pyramids, it appears to thread along the [0001] direction, which is the direction of growth.

Dislocations such as the one outlined by the black circle (labelled "D") are probably dislocations which initially propagate in the *c*-/[0001] direction and then bend by 90° and thread to the surface along the $[10\bar{1}0]$ direction.[12,44] Dislocation bending is observed when they propagate sufficiently close to a free surface in order to minimize their energy, as observed in epitaxial lateral overgrowth, for example.[45,46] Figure 5(b) appears to show one of these dislocations with an additional dislocation segment "E" propagating approximately in the $[10\bar{1}2]$ direction.

Dislocation "F" appears to initially propagate in the $[1\bar{2}10]$ direction in the (0001) plane, then propagates in the $[2\bar{1}\bar{1}0]$ direction in possibly the (0001) or $(1\bar{1}01)$ plane,[43] and then in the $[1\bar{2}10]$ direction in the (0001) plane. Dislocations C, E, and F may all be threading arms of misfit dislocations, propagating in different directions, but all are lying in the (0001) plane.

IV. CONCLUSIONS

In summary, GaN was grown by MOCVD on (113) Si substrates, which had been patterned into periodic stripes to expose {111} sidewalls. Growth of (0001)-orientated GaN from opposing {111} Si surfaces then led to the formation of GaN structures with "bow-tie" shaped cross-section and two inclined $(10\bar{1}1)$ top surface facets with InGaN/GaN MQWs grown on top. Room temperature CL imaging revealed two types of defects causing nonradiative recombination: black spots in GaN intensity images and dark lines in CL intensity images of the MQW emission. Further investigation using ECCI identified the black spots as threading dislocations propagating to the inclined surface. The line defects, also seen in the MQW intensity images, are identified as misfit dislocations, which are caused by glide in basal (0001) planes at the interfaces of the MQW structure. They propagate along the $[1\bar{2}10]$ direction parallel to the stripes in the patterned Si substrate and can also bend and propagate with different line directions in the (0001) plane. These defects could be positively identified as misfit dislocations associated with the MQW structure because they are only present in the CL images of the MQW emission, but not in those of the GaN emission. Furthermore, CL imaging at low temperature showed additional emission lines at energies below that of the GaN bound exciton. They are most likely linked to extended defects such as basal-plane stacking faults, prismatic stacking faults, and

partial dislocations at either the GaN/Si interface or the join of the bow-tie [where the two (0001) growth fronts meet]; donor–acceptor pair transitions; or zinc-blende inclusions. Overall, combining nondestructive structural and luminescence imaging techniques can provide valuable complementary information on structural defects and their emission properties.

SUPPLEMENTARY MATERIAL

Further results on electron backscatter diffraction (EBSD), high resolution X-ray diffraction (HRXRD), cross-sectional cathodoluminescence (CL), and transmission electron microscopy (TEM) measurements are available in Secs. S1, S2, S3, and S4, respectively, of the supplementary material.

ACKNOWLEDGMENTS

The authors would like to acknowledge the Engineering and Physical Sciences Research Council (U.K.) [EPSRC(GB)] (Grant Nos. EP/L016982/1, EP/M003132/1, EP/P015719/1, EP/P006973/1, and EP/M015181/1) for financial support. J. Bruckbauer acknowledges the support of SUPA through a PECRE travel award.

The data associated with this research are available at https://doi.org/10.15129/c71c237d-a544-4bf5-b7d3-1432ea22608e or from the corresponding author.

REFERENCES

[1]P. K. Bondyopadhyay, Proc. IEEE **86**, 78 (1998).
[2]M. M. Waldrop, Nature **530**, 144 (2016).
[3]R. Haitz, *Advances in Solid State Physics*, edited by B. Kramer (Springer, 2003), Vol. 43, pp. 35–50.
[4]O. Ambacher, J. Majewski, C. Miskys, A. Link, M. Hermann, M. Eickhoff, M. Stutzmann, F. Bernardini, V. Fiorentini, V. Tilak, B. Schaff, and L. F. Eastman, J. Phys. Condens. Matter **14**, 3399 (2002).
[5]A. E. Romanov, T. J. Baker, S. Nakamura, and J. S. Speck, J. Appl. Phys. **100**, 023522 (2006).
[6]P. Waltereit, O. Brandt, A. Trampert, H. T. Grahn, J. Menniger, M. Ramsteiner, M. Reiche, and K. H. Ploog, Nature **406**, 865 (2006).
[7]M. Feneberg, F. Lipski, R. Sauer, K. Thonke, T. Wunderer, B. Neubert, P. Brückner, and F. Scholz, Appl. Phys. Lett. **89**, 242112 (2006).
[8]D. Zhu, D. J. Wallis, and C. J. Humphreys, Rep. Prog. Phys. **76**, 106501 (2013).
[9]X. Yu, "MOCVD growth of novel GaN materials on silicon substrates," Ph.D. thesis (School University of Sheffield, 2017).
[10]H. Ibach, H. D. Bruchmann, and H. Wagner, Appl. Phys. A **29**, 113 (1982).
[11]M. Khoury, O. Tottereau, G. Feuillet, P. Vennéguès, and J. Zúñiga-Pérez, J. Appl. Phys. **122**, 105108 (2017).
[12]R. Mantach, P. Vennéguès, J. Zuniga Perez, P. De Mierry, M. Leroux, M. Portail, and G. Feuillet, J. Appl. Phys. **125**, 035703 (2019).
[13]A. Dadgar, J. Bläsing, A. Diez, A. Alam, M. Heuken, and A. Krost, Jpn. J. Appl. Phys. **39**, L1183 (2000).
[14]D. Zhu, C. McAleese, M. Häberlen, C. Salcianu, T. Thrush, M. Kappers, A. Phillips, P. Lane, M. Kane, D. Wallis, T. Martin, M. Astles, N. Hylton, P. Dawson, and C. Humphreys, J. Appl. Phys. **109**, 014502 (2011).
[15]N. Izyumskaya, S. J. Liu, V. Avrutin, X. F. Ni, M. Wu, U. Özgür, S. Metzner, F. Bertram, J. Christen, L. Zhou, D. J. Smith, and H. Morkoç, J. Cryst. Growth **314**, 129 (2011).
[16]J. Bruckbauer, P. R. Edwards, T. Wang, and R. W. Martin, Appl. Phys. Lett. **98**, 141908 (2011).
[17]P. R. Edwards, L. K. Jagadamma, J. Bruckbauer, C. Liu, P. Shields, D. Allsopp, T. Wang, and R. W. Martin, Microsc. Microanal. **18**, 1212 (2012).
[18]M. Hocker, P. Maier, I. Tischer, T. Meisch, M. Caliebe, F. Scholz, M. Mundszinger, U. Kaiser, and K. Thonke, J. Appl. Phys. **121**, 075702 (2017).
[19]C. Trager-Cowan, F. Sweeney, P. W. Trimby, A. P. Day, A. Gholinia, N.-H. Schmidt, P. J. Parbrook, A. J. Wilkinson, and I. M. Watson, Phys. Rev. B **75**, 085301 (2007).
[20]G. Naresh-Kumar, D. Thomson, M. Nouf-Allehiani, J. Bruckbauer, P. Edwards, B. Hourahine, R. Martin, and C. Trager-Cowan, Mater. Sci. Semicond. Proc. **47**, 44 (2016).
[21]G. Naresh-Kumar, C. Mauder, K. R. Wang, S. Kraeusel, J. Bruckbauer, P. R. Edwards, B. Hourahine, H. Kalisch, A. Vescan, C. Giesen, M. Heuken, A. Trampert, A. P. Day, and C. Trager-Cowan, Appl. Phys. Lett. **102**, 142103 (2013).
[22]K. Nauka, G. A. Reid, and Z. Liliental-Weber, Appl. Phys. Lett. **56**, 376 (1990).
[23]G. Naresh-Kumar, J. Bruckbauer, P. R. Edwards, S. Kraeusel, B. Hourahine, R. W. Martin, M. J. Kappers, M. A. Moram, S. Lovelock, R. A. Oliver, C. J. Humphreys, and C. Trager-Cowan, Microsc. Microanal. **20**, 55 (2014).
[24]S. Srinivasan, L. Geng, R. Liu, F. A. Ponce, Y. Narukawa, and S. Tanaka, Appl. Phys. Lett. **83**, 5187 (2003).
[25]M. T. Hardy, P. S. Hsu, F. Wu, I. L. Koslow, E. C. Young, S. Nakamura, A. E. Romanov, S. P. DenBaars, and J. S. Speck, Appl. Phys. Lett. **100**, 202103 (2012).
[26]A. M. Smirnov, E. C. Young, V. E. Bougrov, J. S. Speck, and A. E. Romanov, APL Mater. **4**, 016105 (2016).
[27]T. Tanikawa, T. Sano, M. Kushimoto, Y. Honda, M. Yamaguchi, and H. Amano, Jpn. J. Appl. Phys. **52**, 08JC05 (2013).
[28]C. Hums, T. Finger, T. Hempel, J. Christen, A. Dadgar, A. Hoffmann, and A. Krost, J. Appl. Phys. **101**, 033113 (2007).
[29]A. Billeb, W. Grieshaber, D. Stocker, E. F. Schubert, and R. F. Karlicek, Jr., Appl. Phys. Lett. **70**, 2790 (1997).
[30]J. Lähnemann, U. Jahn, O. Brandt, T. Flissikowski, P. Dogan, and H. T. Grahn, J. Phys. D **47**, 423001 (2014).
[31]R. Liu, A. Bell, F. A. Ponce, C. Q. Chen, J. W. Yang, and M. A. Khan, Appl. Phys. Lett. **86**, 021908 (2005).
[32]P. P. Paskov, R. Schifano, B. Monemar, T. Paskova, S. Figge, and D. Hommel, J. Appl. Phys. **98**, 093519 (2005).
[33]J. Bai, M. Dudley, L. Chen, B. J. Skromme, B. Wagner, R. F. Davis, U. Chowdhury, and R. D. Dupuis, J. Appl. Phys. **97**, 116101 (2005).
[34]J. Mei, S. Srinivasan, R. Liu, F. A. Ponce, Y. Narukawa, and T. Mukai, Appl. Phys. Lett. **88**, 141912 (2006).
[35]I. Tischer, M. Feneberg, M. Schirra, H. Yacoub, R. Sauer, K. Thonke, T. Wunderer, F. Scholz, L. Dieterle, E. Müller, and D. Gerthsen, Phys. Rev. B **83**, 035314 (2011).
[36]M. Hocker, I. Tischer, B. Neuschl, K. Thonke, M. Caliebe, M. Klein, and F. Scholz, J. Appl. Phys. **119**, 185703 (2016).
[37]M. A. Reshchikov and H. Morkoç, J. Appl. Phys. **97**, 061301 (2005).
[38]J. Menniger, U. Jahn, O. Brandt, H. Yang, and K. Ploog, Phys. Rev. B **53**, 1881 (1996).
[39]S. D. Carnevale, J. I. Deitz, J. A. Carlin, Y. N. Picard, M. De Graef, S. A. Ringel, and T. J. Grassman, Appl. Phys. Lett. **104**, 232111 (2014).
[40]L. Jian-Ming, Z. Jie, L. Wen-Yu, Y. Meng-Xin, F. Xiang-Xu, Z. Dong-Yan, S. Ding, X. Chen-Ke, and L. Bao-Lin, Chin. Phys. B **24**, 057801 (2015).
[41]L. Schade, T. Wernicke, J. Raß, S. Ploch, M. Weyers, M. Kneissl, and U. T. Schwarz, Phys. Status Solidi A **211**, 756 (2014).
[42]A. E. Romanov, E. C. Young, F. Wu, A. Tyagi, C. S. Gallinat, S. Nakamura, S. P. DenBaars, and J. S. Speck, J. Appl. Phys. **109**, 103522 (2011).
[43]M. Hiraiwa, F. Liu, S. Shibata, S. Takeda, Y. Tsusaka, Y. Kagoshima, and J. Matsui, Jpn. J. Appl. Phys. **54**, 025503 (2015).
[44]M. Khoury, P. Vennéguès, M. Leroux, V. Delaye, G. Feuillet, and J. Zúñiga-Pérez, J. Phys. D **49**, 475104 (2016).
[45]P. Vennéguès, B. Beaumont, V. Bousquet, M. Vaille, and P. Gibart, J. Appl. Phys. **87**, 4175 (2000).
[46]S. Gradečak, P. Stadelmann, V. Wagner, and M. Ilegems, Appl. Phys. Lett. **85**, 4648 (2004).